Sub-core scale fluid flow behavior in a sandstone with cataclastic deformation bands

Carla R. Romano[1]†, Christopher Zahasky[2], Charlotte Garing[3], James M. Minto[1], Sally M. Benson[4], Zoe K. Shipton[1], Rebecca J. Lunn[1]

[1]Department of Civil and Environmental Engineering, University of Strathclyde, Glasgow, UK

[2]Department of Geoscience, University of Wisconsin-Madison, Madison, WI, US

[3]Department of Geology, University of Georgia, Athens, GA, US

[4]Department of Energy Resources Engineering, School of Earth Sciences, Stanford University, Stanford, USA

Corresponding author: Carla R. Romano (carla.romano@strath.ac.uk)

†Current address: James Weir Building, 75 Montrose Street, G1 1XJ, Glasgow, UK

ORCID iDs

Carla R. Romano https://orcid.org/0000-0001-5082-951X
Christopher Zahasky https://orcid.org/0000-0002-3427-5622
Charlotte Garing https://orcid.org/0000-0001-8767-7847
James M. Minto https://orcid.org/0000-0002-9414-4157
Sally M. Benson https://orcid.org/0000-0002-3733-4296
Zoe K. Shipton https://orcid.org/0000-0002-2268-7750
Rebecca J. Lunn https://orcid.org/0000-0002-4258-9349

Key Points:

- Cataclastic deformation bands strongly influence the fluid velocity field in a single phase core flooding experiment.
- Cataclastic deformation bands produce capillary barriers that severely limit cross flow between host rock compartments.
- The impact of deformation bands, laminae, and experimental boundary conditions are analyzed using numerical simulations.

Abstract

Accurate determination of petrophysical and multiphase flow properties in sandstones is necessary for reservoir characterization, for instance for carbon dioxide and hydrogen storage in geological formations or for enhanced oil recovery. Several studies have examined the effect of heterogeneities, such as fractures, bedding planes and laminae, on core-scale fluid flow. However, the influence of deformation bands that commonly occur in high porosity sandstones, is poorly understood. In this study, we consider a core sample of Navajo sandstone characterized by diagonally oriented deformation bands and two laminae perpendicular to the core axis, as determined from micro X-ray computed tomography (micro-CT). Positron emission tomography (PET) is used to derive the single phase hydrodynamic properties of the core. A CO_2 drainage experiment is conducted in the water-saturated core and imaged with a medical X-ray CT scanner. Medical CT enables CO_2 saturation quantification with increasing CO_2 injection rate. Experimental results and the accompanying numerical simulations indicate that both the laminae and the deformation bands act as capillary barriers, with the laminae forming weaker capillary barriers than the deformation bands. The deformation bands have lower permeability and porosity due to grain crushing, and a very high capillary entry pressure that inhibits CO_2 migration across the bands. At the reservoir scale, deformation bands form conjugate sets and are often present in thick anastomosing clusters that define lozenge-shaped compartments. These findings have important consequences for subsurface fluid flow. For example, the presence of deformation bands may reduce the storage capacity and injectivity in carbon storage reservoirs.

Keywords: deformation bands, multiphase fluid flow, capillary heterogeneity, X-ray computed tomography, positron emission tomography

Index terms: Rocks: physical properties, Groundwater transport.

1 Introduction

Sandstones are one of the most high quality and high storage volume candidate geological formations for gas storage due to their global distribution, and high porosity and permeability (Benson & Cook, 2005; Bjørlykke & Jahren, 2010). Key to realizing their potential will be an accurate assessment of their reservoir-scale petrophysical properties and multiphase flow characteristics. These properties govern the behavior of multiphase fluids within the rock and hence will determine the efficiency of injection projects such as carbon dioxide storage, hydrogen storage, and enhanced oil recovery schemes.

Together with field observations, laboratory core flooding experiments are a valuable tool for determining petrophysical properties and multiphase flow characteristics under reservoir conditions. Integrating experiments with advanced imaging techniques, such as X-ray computed tomography (CT) and positron emission tomography (PET), enables measurement of single and multiphase flow properties from the pore-scale to the centimeter-scale. In X-ray CT, an X-ray beam is generated, and attenuation values are determined based on the electron density of materials within the sample (Kruth, et al., 2011). This allows the spatial distribution of fluids with differing densities to be determined (Akin & Kovscek, 2003). Both medical CT and micro-CT are commonly used in Earth science. Medical CT is able scan centimeter-scale samples in minutes with millimeter resolution while micro-CT provides micrometer-scale images with scans that take several hours. PET imaging, by contrast, relies on the detection of photons from positron-emitting

radiotracers that are injected into the rock. Detection of the photons enables time-resolved quantification of radiotracer migration through the sample. Thus with PET imaging it is possible to quantify fluid transport behavior, while CT provides high-resolution information about rock structure and fluid saturation distribution (Pini, et al., 2012; Zahasky, et al., 2019).

Imaging and analysis of core flooding experiments enables quantification of rock and fluid properties, such as porosity and absolute permeability (Krause, et al., 2013; Ochi & Vernoux, 1998; Perrin, et al., 2009; Zahasky & Benson, 2018), fluid saturation, capillary pressure and relative permeability (Akbarabadi & Piri, 2013; Krevor, et al., 2012; Pini, et al., 2012; Ruprecht, et al., 2014; Vinegar & Wellington, 1987). Many of these studies indicated that sandstones are characterized by subtle small-scale heterogeneities that actively affect fluid flow. Variations in porosity and permeability affect the fluid velocity field, with high velocities being associated with regions of high porosity and permeability (Bloomfield, et al., 2001; Grathwohl & Kleineidam, 1995; Vasco, et al., 2018; Zahasky & Benson, 2018) and for multiphase fluid flow, variations in capillary pressure and relative permeability affect plume migration and residual saturation at both the pore and the field scale (Hingerl, et al., 2016; Krevor, et al., 2012; Krevor, et al., 2015; Li & Benson, 2015; Perrin & Benson, 2010; Pini & Benson, 2017; Saadatpoor, et al., 2010). In particular, Krevor et al. (2011) reported that regions presenting high capillary entry pressures (i.e. small pore throats) act as capillary barriers for the non-wetting fluid, leading to an increase in saturation of the latter in the preceding pores.

Until now, sub-core scale flow and transport behavior in heterogeneous porous media has focused on sandstones characterized by the presence of bedding planes, laminae and/or fractures (Corey & Rathjens, 1956; Hingerl, et al., 2016; Kim, et al., 2018; Krevor, et al., 2011; Li, et al., 2019; Manzocchi, et al., 2002; Medina, et al., 2011; Pasala, et al., 2013; Shipton, et al., 2002; Tueckmantel, et al., 2012). Relatively little attention has been given to experimentally understanding the impact of deformation bands on fluid flow. Deformation bands are low porosity bands that form in response to shear and they are extremely common in sandstones with a porosity greater than 0.15 (Aydin, 1978; Fossen, et al., 2007; Schultz & Siddharthan, 2005). Several types of deformation bands can be defined based on their kinematic mechanisms. The most common are compactional shear or cataclastic bands (Aydin, et al., 2006). These form by a combination of shear and compaction mechanisms and are always characterized by cataclasis. Cataclastic bands are millimeters thick tabular structures (Aydin, 1978; Aydin & Johnson , 1978), along which grain rolling and grain fracturing lead to a reduced porosity and permeability. Multiple studies have reported that deformation bands are several orders of magnitude less permeable than the host rocks in which they form (Antonellini & Aydin, 1994; Aydin & Johnson , 1978; Ballas, et al., 2015; Fossen, et al., 2007; Taylor & Polland, 2000). A single band can accommodate only a few millimeters of displacement; upon further deformation, rather than continuously slipping, a pre-existing band experiences strain hardening (Aydin & Johnson , 1978; Shipton & Cowie, 2003). As a result, new bands form to accommodate additional strain. This is why conjugate sets or anastomosing clusters of deformation bands are common.

Cataclastic bands usually form at burial depths greater than 1 km, but there is evidence of their presence at shallower burial depths in unconsolidated sandstones (Cashman & Cashman, 2000; Rawling & Goodwin, 2003). They are often found in fault damage zones, i.e. in the volume of rock that accommodates deformation during initiation and propagation of slip along fault (McGrath & Davison, 1995; Rotevatn & Fossen, 2011; Shipton & Cowie, 2001; Shipton & Cowie,

2003). Since deformation bands are well below the resolution of seismic data, their extent within the damage zone is not easy to predict (sub-seismic faults are generally faults with an offset of < 10 m that cannot be detected using seismic reflection data, although strike slip faults of much larger offsets are also not resolvable). Moreover, it has been found that no relationship exists between fault displacement and frequency of deformation bands (Schueller, et al., 2013): the same frequency of deformation bands may be associated with seismically resolvable faults and sub-seismic faults.

It is highly likely that deformation bands will be present in most high porosity sandstone reservoirs, hence understanding how they influence fluid flow, and determining their petrophysical properties, is key to accurate reservoir characterization. Several studies have highlighted how deformation bands can negatively affect fluid flow, leading to pressure compartmentalization, a higher degree of tortuosity, fluid bypass and a lower than expected reservoir permeability (Ogilvie, et al., 2001; Qu & Tveranger, 2016; Rotevatn & Fossen, 2011; Rotevatn, et al., 2017; Schultz & Siddharthan, 2005; Shipton, et al., 2002; Shipton, et al., 2005; Wilkins, et al., 2019). However, most of these studies have relied on results from reservoir simulations and analysis of field data. Here, we present the first *in situ* visualization and quantification of sub-core scale single phase and multiphase fluid flow experiments in a sandstone rock core that contains deformation bands and fine-grained laminae. Laminae are mm-thick sedimentary layers forming due to episodic changes in depositional energy (Campbell, 1967). Single phase flow experiments were conducted using PET imaging. Multiphase flow experiments were performed by injecting CO_2 into a water saturated rock sample and acquiring several consecutive medical X-ray CT scans. Our results demonstrate that deformation bands significantly influence single phase flow and that in a multiphase flow setting, they have a profound effect on fluid phase distribution within the rock.

2 Methodology

The 5 cm diameter, 10 cm long rock core used in this study was retrieved from a borehole depth of 57 m in the Navajo sandstone formation. The borehole was drilled into the hanging wall of the Big Hole normal fault, in the north of the San Rafael Swell, Utah (Shipton, et al., 2002). The core was sampled from the 17 m thick damage zone that surrounds the Big Hole Fault at this location. The host rock is characterized as a fine-grained sandstone with cataclastic deformation bands (Figure 1a).

2.1 Micro-CT

To characterize the geometry of the deformation bands, the core was scanned at the University of Strathclyde with an X-ray micro-CT scanner (Nikon XT H 225 LC) that produced three-dimensional (3D) tomographic images with a voxel size of 0.029x0.029x0.029 mm. The above mentioned facility was, however, not available for imaging during the core flooding experiments. Core flooding experiments were conducted at Stanford University using medical CT and PET imaging. The high-resolution micro-CT images provide more detailed information on the deformation band geometries that could not be inferred by the lower resolution of medical CT and PET scanner.

2.2 *Porosity characterization*

The 3D porosity distribution within the core was determined using a medical X-ray CT scanner (General Electric Hi-Speed CT/i) at Stanford University. Image acquisition was performed at 120

kV and 200 mA, obtaining a voxel dimension of 0.3125x0.3125x0.625 mm. Images of the core were taken when fully dry (CT_{dry}) and when fully water saturated (CT_{water}). The porosity, Φ, was then calculated using the following relationship (Withjack, 1988; Akin & Kovscek, 2003):

$$\Phi = \frac{CT_{water} - CT_{dry}}{I_{water} - I_{air}} \quad (1)$$

where *I water* and *I air* are the water and air X-ray attenuation values respectively, which differ by 1000 Hounsfield units (Wellington & Vinegar, 1987). To reduce noise in CT images at least three series for each condition were acquired and averaged (Pini, et al., 2012). The images of the entire core were discretized into 38x38x76 cells, each with a dimension of 0.125 cm.

2.3 *Single phase permeability characterization*

Bulk intrinsic permeability was determined using the core-flooding set-up described in the section 2.4 and under the same conditions of temperature, pressure and confining pressure as for the multiphase flow experiment. Injecting water at several flow rates into the water saturated core sample and measuring corresponding differential pressure across the core, allowed permeability calculation with Darcy's Law.

To investigate the 3D distribution of permeability within the core, a tracer experiment was conducted within the micro-PET scanner (Siemens Inveon D-PET) using the experimental setup described in Zahasky & Benson (2018). Before fluid injection, the core was wrapped in two heat-shrinkable Teflon layers and a rubber sleeve to avoid any leakage of the confining fluids into the core. The core was then placed in an aluminum core holder with inlet and outlet caps etched with a pattern of connected grooves for an even distribution of injected fluids. Finally, the core holder was placed in the micro-PET scanner and connected to the core flooding equipment.

To ensure full core water saturation, the core was first dried. CO_2 was then injected to displace the air, followed immediately by water that was injected for displacing and dissolving the CO_2. Once the core was fully saturated, a solution of Fludeoxyglucose (^{18}F-FDG) diluted in tap water was injected at 4 mL/min. The approximate radioactive concentration was 0.52 mCi/mL. Throughout the experiment a PET scan continuously acquired photon detection data. The experiment was carried out at a constant temperature of 20 °C, with a confining pressure of 2.4 MPa. The back pressure was maintained just above atmospheric pressure.

To calculate the 3D concentration field of the radiotracer within the core, the PET scan data was reconstructed with a time-step length of 40 seconds. The image-based core was discretized into a grid of 22x22x42 cells giving a voxel size for each concentration measurement of 0.23x0.23x0.23 cm. Analyzing concentration measurements as a function of time from the PET scans, enables estimates of the mean arrival time and fluid velocity at any location within the core. The radiotracer concentration in each voxel over time was fitted with a first order Gaussian function to remove background noise (Vasco, et al., 2018). The total mass of radiotracer was calculated for each voxel using the temporal zero moment equation

$$M0 = \int_0^t c\, dt \quad (2)$$

where c is the radiotracer concentration in each voxel. The mean arrival time is identified as the center of mass of the Gaussian function and calculated with the temporal first moment equation (Naff, 1990).

$$M1 = \int_0^t ct\, dt \tag{3}$$

The normalized first moment then defines the mean arrival time of the plume center.

$$nM1 = \frac{M1}{M0} \tag{4}$$

Knowing the distance between two adjacent units, i.e. the distance between voxels, a map of the velocity field can be derived. The velocity is normalized, enforcing a mass balance, by setting the total flow rate of each cross-sectional slice within the core equal to the inflow rate that we imposed in the experiment (4 mL/min). This analysis assumes flow is parallel to the axis of the core, a good approximation as the cylindrical faces of the core were no-flow boundaries.

2.4 Multiphase core flooding experiments

To determine the multiphase flow properties of the rock core, CO_2/water drainage capillary pressure experiments (Pini, et al., 2012) at steady-state conditions were conducted at 25 °C and 9 MPa, with a confining pressure of 11 MPa. Drainage is the process of displacing the wetting phase (water) with non-wetting phase (CO_2). Near ambient temperature was used here because previous studies have shown that temperature has no influence on the saturation end point when CO_2 is injected in a water saturated sample (Niu, et al., 2015). The core flooding setup is similar to the one used in previous experiments (Krevor, et al., 2012; Ni, et al., 2019; Perrin & Benson, 2010) and details can be found in supporting information (Text S1, Figure S1). The core was not fired before the experiment, due to the low clay content (Shipton, et al., 2002) and because previous studies have shown that firing in CO_2/water/sandstone (with low clay content) system does not change experimental results and wetting properties (Garing & Benson, 2019). The core was first dried in the oven for several days and then wrapped using the same layering protocol as for the single phase experiment (section 2.3). Considering that CO_2 can permeate through Teflon, an additional layer of aluminum foil has been placed between the Teflon layers to avoid any radial diffusion of CO_2 out of the rock core. The core was then placed in an aluminum core holder and connected to a core flooding setup suitable for conducting high pressure and temperature-controlled experiments.

Before CO_2 injection, the rock core was fully saturated with water that had been pre-equilibrated with CO_2 at the experimental conditions. For the drainage experiment, 100% CO_2 was continuously injected at progressively higher flow rates, from 0.3 mL/min to 20 mL/min. At these conditions the capillary number $Ca = \frac{v\,\mu_{CO2}}{\gamma}$ ranges from 10^{-7} to 10^{-8}, where v is the fluid velocity (m/s), $\mu_{CO2} = 7.06 \times 10^{-5}$ (Pa ·s) is the viscosity of the CO_2 at experimental conditions and γ = 35 (mN/m) is the CO_2/water interfacial tension. This suggests that capillary forces dominate over viscous forces in this system. A Bond number, $Bo = \frac{\Delta\rho g L^2}{\gamma}$ (density difference $\Delta\rho$ of 201 kg·m^{-3} and a pore length L of 50 micron) on the order of 10^{-5} indicates that buoyancy forces are smaller compared to capillary forces.

229 At each flow rate each flow rate, a minimum of 5 PV (1 PV = 38 mL) of CO_2 were injected to
230 ensure steady state was reached (Perrin, et al., 2009). Once steady state conditions were reached,
231 the medical X-ray CT scanner (section 2.2) was used for obtaining scan images of the CO_2
232 saturated core, water saturated core and partially saturated core with a voxel size of
233 0.3125x0.3125x0.625 mm. CO_2 saturation (S_{CO_2}) is measured using the following formula (Akin
234 & Kovscek, 2003):

235 $$S_{CO_2} = \frac{CT_{exp} - CT_{wat\ sat}}{CT_{CO2\ sat} - CT_{wat\ sat}} \quad (5)$$

236 where $CT_{wat\ sat}$ are scan images taken when the core was fully saturated with equilibrated water,
237 $CT_{CO2\ sat}$ are the scan images of the fully CO_2 saturated core. For each condition, at least three
238 series of scans were taken; and the average of the three was computed for reducing uncertainties
239 on saturation results (Pini, et al., 2012). The resulting images were then coarsened for further noise
240 reduction, obtaining a final voxel resolution of 0.125x0.125x0.125 cm.

241 Capillary pressure at the inlet portion of the core was measured for each flow rate as the difference
242 between the core inlet and outlet pressure readings. This assumes that during steady state CO_2
243 injection the pressure recorded at the inlet is the CO_2 pressure and the pressure recorded at the
244 outlet is the water pressure (Pini, et al., 2012).

245 **3 Results**

246 *3.1 Deformation band geometry*

247 Figures 1a and 1b show a photograph of the core alongside a 3D image of the distribution of
248 attenuation values from the X-ray micro-CT scanner: higher attenuation values, in white,
249 correspond to higher density materials. A deformation band is clearly visible in both images
250 traversing the full sample horizontally from end-to-end, at an angle of approximately 18° to the
251 long-axis of the core. Two core-perpendicular laminae of finer grained material are also apparent
252 in the micro-CT scan (Figure 1b). Analysis of sequential cross-sectional slices in the X-ray micro-
253 CT scan (Figures 1c-1f) show that, rather than a single band, there are two bands. These offset the
254 first and second laminae by 3 mm and 5 mm respectively in the slice shown in Figures 1c and 1e.
255 On all the X-ray micro-CT slices, the two main deformation bands are separated by host rock and
256 therefore they do not isolate any portion of the core (Figure 1d). Toward the end of the core (Figure
257 1f), only one deformation band is present, which takes the form of a small anastomosing cluster.

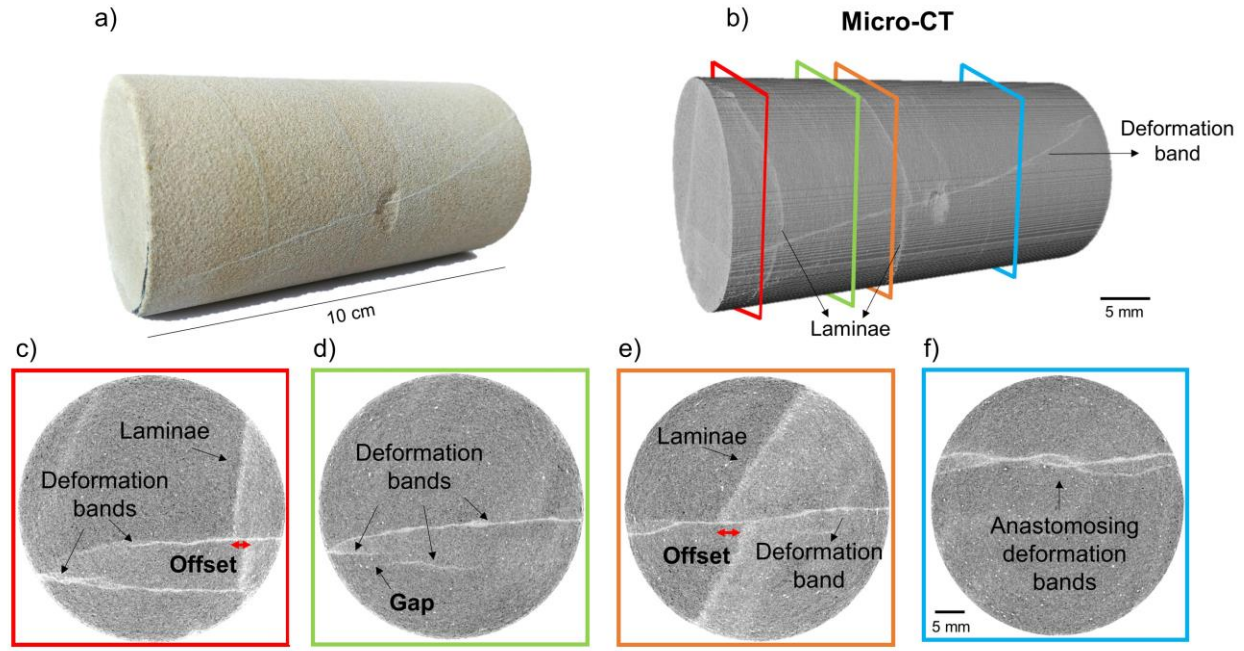

Figure 1. a) Sandstone core sample with cataclastic diagonal deformation band. b) 3D micro-CT scan of the sandstone core: the sample is characterized by a cataclastic deformation band and laminae. Raw data are available in the data repository cited in the Acknowledgments. c) 2D Slice image showing that the two deformation bands offset the first lamina by 3 mm. Deformation bands do not connect to each other on the left side of the image. d) A third deformation band appears in this slice. The bands are not joined and hence they do not form any isolated compartments. e) Second lamina cut by a single deformation band. Offset of about 5 mm. f) Small anastomosing network of deformation bands at the end of the core.

3.2 Porosity distribution

The distribution of porosity within the core, based on the dry and water saturated medical X-ray CT scans (section 2.2), is shown in Figure 2. The deformation bands and laminae are clearly visible as low porosity features. Bulk porosity of the core was calculated as 0.196. Deformation band porosity ranges from 0.07 to 0.15, while porosity of laminae varies from 0.13-0.15.

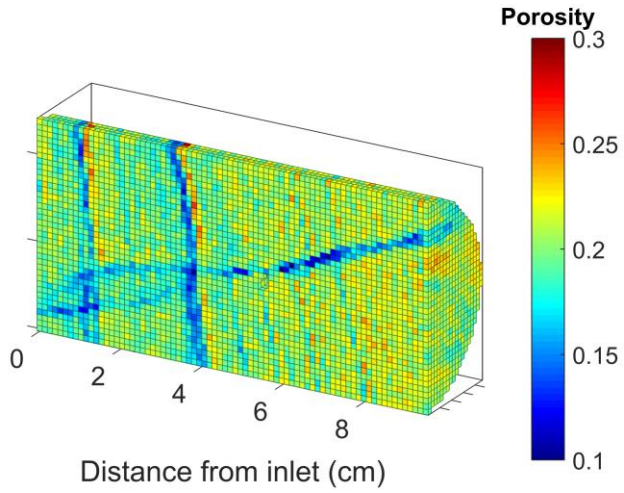

Figure 2. Porosity map calculated by using water saturated and dry scan images with the medical X-Ray CT scanner. Voxel resolution 0.125x0.125x0.125 cm. An uncertainty (σ_φ) of 0.0082 in voxel porosity due to random error of CT number was calculated using methods explained in Pini et al. (2012).

3.3 Intrinsic permeability

Based on measurement of the inlet and outlet pressures at a constant flow rate, a bulk sample permeability of 53 mD was estimated using Darcy's Law. The heterogeneous distribution of permeability within the core was investigated using the PET scanner. Figure 3 shows the concentrations of the single phase radiotracer injection experiment during six different timeframes of the PET scan taken at consecutive 2-minute intervals. Stylized deformation bands and laminae (derived from the micro-CT images) have been superimposed on the PET images to illustrate their effect on the tracer plume migration. Results show that the tracer plume above and below the bands is beginning to diverge 4 min after the start of injection. This effect is more pronounced with increasing distance from the inlet. There is a very low radiotracer concentration in the volume of rock that immediately surrounds the bands.

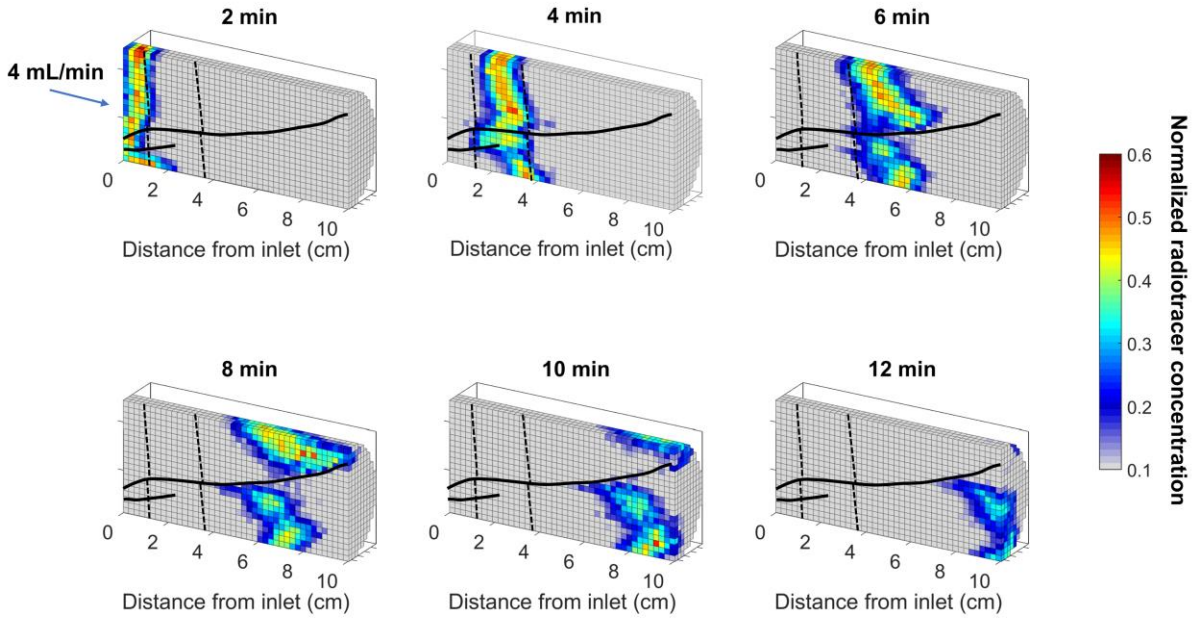

Figure 3. Axial plane snapshots of radiotracer concentration measured at 2-minute time intervals after injection at 4 mL/min into a sandstone core with deformation bands. The approximate deformation bands (continuous black lines) and laminae (dashed black lines) locations are superimposed on the PET images. Voxel size is 0.23x0.23x0.23 cm.

The 3D map of mean arrival time calculated from the PET images (Figure 4a) shows a significantly delayed arrival time for the portion of the host rock that is below the deformation bands compared to above. In the corresponding 3D map of fluid velocity (Figure 4b) there is a clear distinction between velocity in the rock above and below the deformation bands. These differences are related to the geometry of the deformation band within the sample. The deformation band, along which the estimated velocity is almost zero, subdivides the host rock into two regions. In the upper region, the cross-sectional area decreases towards the outlet and hence, according to the principle of continuity, if the flow rate is held constant, the velocity increases. Vice-versa for the region below the bands, the cross-sectional area increases towards the outlet and, hence, the fluid velocity decreases. In both the estimated mean arrival time (Figure 4a) and the velocity (Figure 4b) maps there is no discernable effect of the two sub-vertical laminae on flow.

To estimate the mean intrinsic permeability for both the host rock and the deformation bands, the PET experiment was modelled numerically using the Stanford University General Purpose Research Simulator software (GPRS) (Cao, 2002; Jiang, 2008; Li, 2011; Boon, et al., 2018; Cao & Aziz, 2002; Krause, 2012; Krause, et al., 2013; Li, et al., 2012; Li & Benson, 2015). Details of model set-up are included in supporting information (Table S1, Figure S2). Multiple combinations of the host rock permeability and deformation band permeability were tested. Each combination had an equivalent bulk core permeability equal to the experimentally measured value of 53 mD. Flow within the core was modelled in 2D, using a grid of 35X78 cells with a grid cell resolution of 0.125 cm, a homogeneous host rock and a single, straight, diagonal deformation band (Figure

4c). The velocity of the fluid for each cell in the simulations was calculated using Darcy's law, assuming an axial flow direction. The simulation results for three combinations of host rock and deformation band permeability are shown in Figure 4c. Specifically, the combinations evaluated were 55 mD and 10 mD, 100 mD and 0.5 mD, 500 mD and 0.0005 mD for the host rock and deformation band respectively. A qualitative comparison of the velocity fields calculated from model simulations with the PET-derived velocity field shows that, although all three models have the same bulk permeability, the local velocity distributions differ. The results for a permeability of 100 mD for the host rock and 0.5 mD for the deformation band most closely resemble the experimental data (Figure 4b).

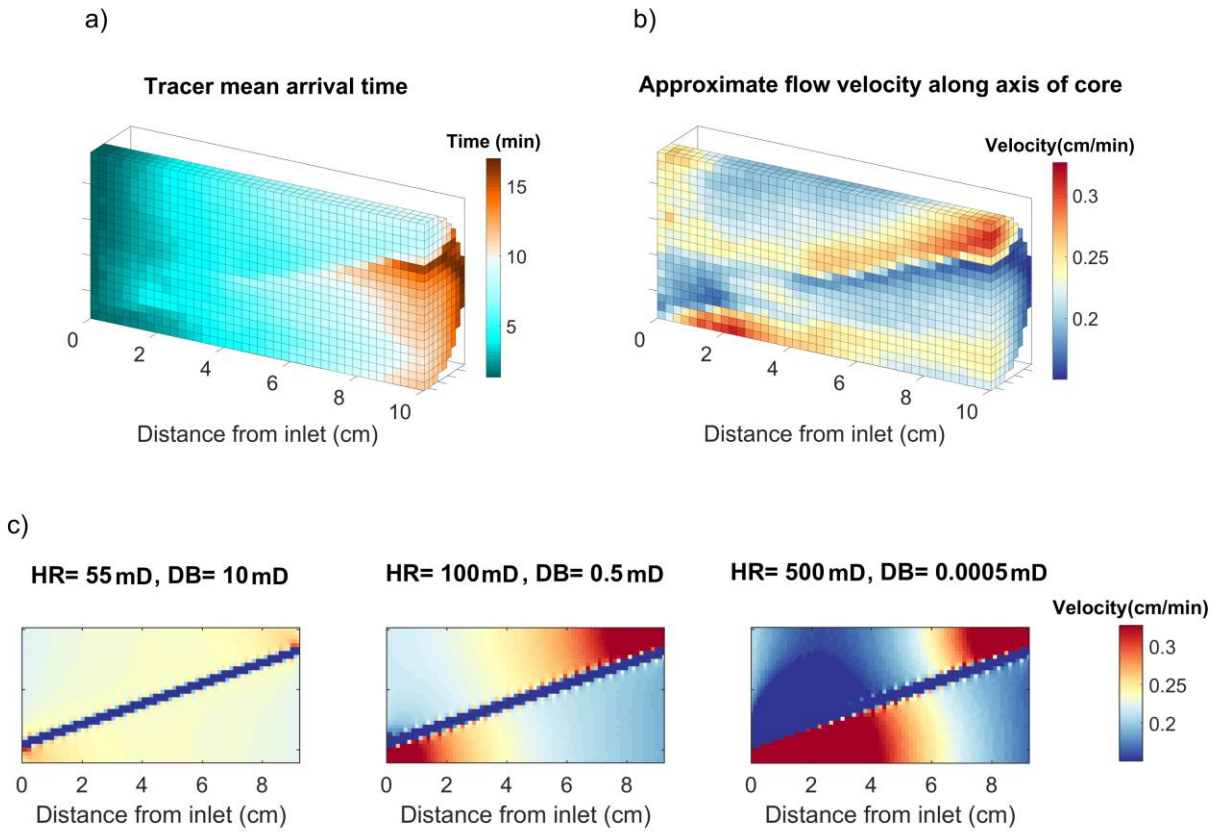

Figure 4. a) Mean arrival time of the radiotracer solution in the sandstone core with deformation bands. Delayed arrival time in compartment below the deformation bands. b) Fluid velocity along the axis of the core calculated from the experimental data. c) Fluid velocity calculated simulating water injection in three pseudo 3D models with different permeability in the host rock (HR) and deformation band (DB). The model with 100 mD in the HR and 0.5 mD in the DB provides the best match with the velocity field obtained in the experiments.

The heterogeneous permeability distribution was estimated using the porosity-permeability relationship proposed by Torabi et al. (2013):

$$k_{HR} = 1e - 9\ {\varphi_{HR}}^{AHR} \quad (6)$$

$$k_{DB} = 2e - 7{\varphi_{DB}}^{ADB} \quad (7)$$

where k_{HR}, φ_{HR}, k_{DB}, φ_{DB} are permeability (mD) and porosity (in percentage) of the host rock and deformation bands respectively and A_{HR} and A_{DB} are dimensionless constants. Among several porosity-permeability relationships, this is preferred considering that it specifically relies on core-plug laboratory measurements of undeformed and deformed samples (single and clusters of bands). For our specific study, porosity for each voxel in the core was taken from the data in Figure 2. The A_{HR} and A_{DB} coefficients found by Torabi et al. (2013) are 9.09 and 6.31, respectively. However, by using these coefficients the resulting bulk core permeability, calculated performing single phase simulations, was 280 mD as opposed to the 53 mD experimentally calculated. The constants A_{HR} and A_{DB} were then fitted by constraining the bulk core permeability to have the measured value of 53 mD and the bulk host rock and deformation band permeabilities to have values of 100 mD and 0.5 mD respectively, as estimated from the analysis shown in Figure 4. This resulted in estimates for the constants A_{HR} and A_{DB} of 8.6 and 5.4 for the host rock and deformation bands respectively. The estimated permeability in each cell is shown in Figure 5.

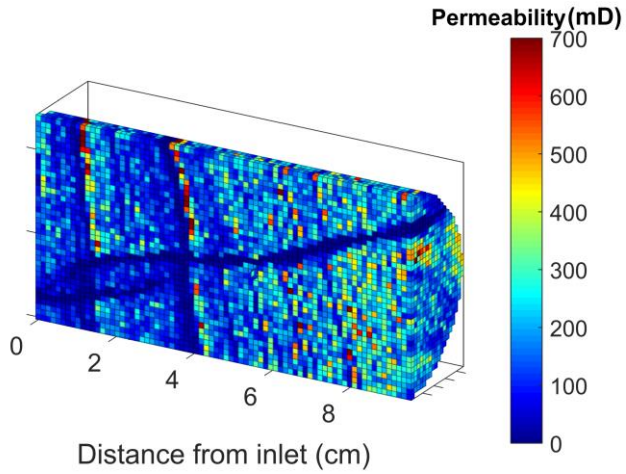

Figure 5. Permeability distribution in millidarcy (mD) calculated using an adapted version of the porosity-permeability relationship found in Torabi et al. *(2013)*.

3.4 Multiphase flow properties

Results of the core flooding CO_2 injection experiments are shown in Figure 6. The injection flow rate was steadily increased in a step-wise fashion over time (Figure 6a). At each step, the flow rate was maintained for a sufficient duration to achieve a steady-state CO_2 saturation distribution (as determined from consecutive medical CT scans). Figure 6b shows that as the flow-rate increases, CO_2 saturation increases in the host rock compartments above and below the deformation bands, but that there remains a lower CO_2 saturation in the compartment below the bands. At low flow rates (0.3 mL/min – 0.6 mL/min – 1 mL/min – 2 mL/min) CO_2 is not able to saturate the outlet of the core below the deformation bands, creating a shadow zone of reduced CO_2 saturation.

Due to their low porosity and permeability and high capillary entry pressure, the deformation bands exhibit low CO_2 saturation, even at high flow rates. Flow across the bands can only occur if the

capillary entry pressure of the bands has been exceeded. Hence, the bands act as capillary barriers and inhibit most flow between the two compartments even at high flow rates.

In contrast to the single phase PET tracer experiment (Figure 3), the laminae have a visible effect on CO_2 distribution, with CO_2 saturation being lower in the laminae than the surrounding host rock. The laminae also act as capillary barriers, although to a lesser extent than the deformation bands. Saturation in the laminae remains lower than in the surrounding rock even when the saturation front has passed through the bands. Only once the flow rate reaches 5 mL/min do the laminae fully saturate and at that point they are no longer clearly visible in the X-ray CT images.

The slice-averaged CO_2 saturation for the individual host rock compartments (Figure 6c) indicates that the CO_2 saturation is lower in the compartment below the bands compared to above the bands. This discrepancy becomes less pronounced at the high flow rates. Despite this, even at 20 mL/min of CO_2 injection, the portion of the core near the inlet shows a lower CO_2 saturation in the compartment below the bands.

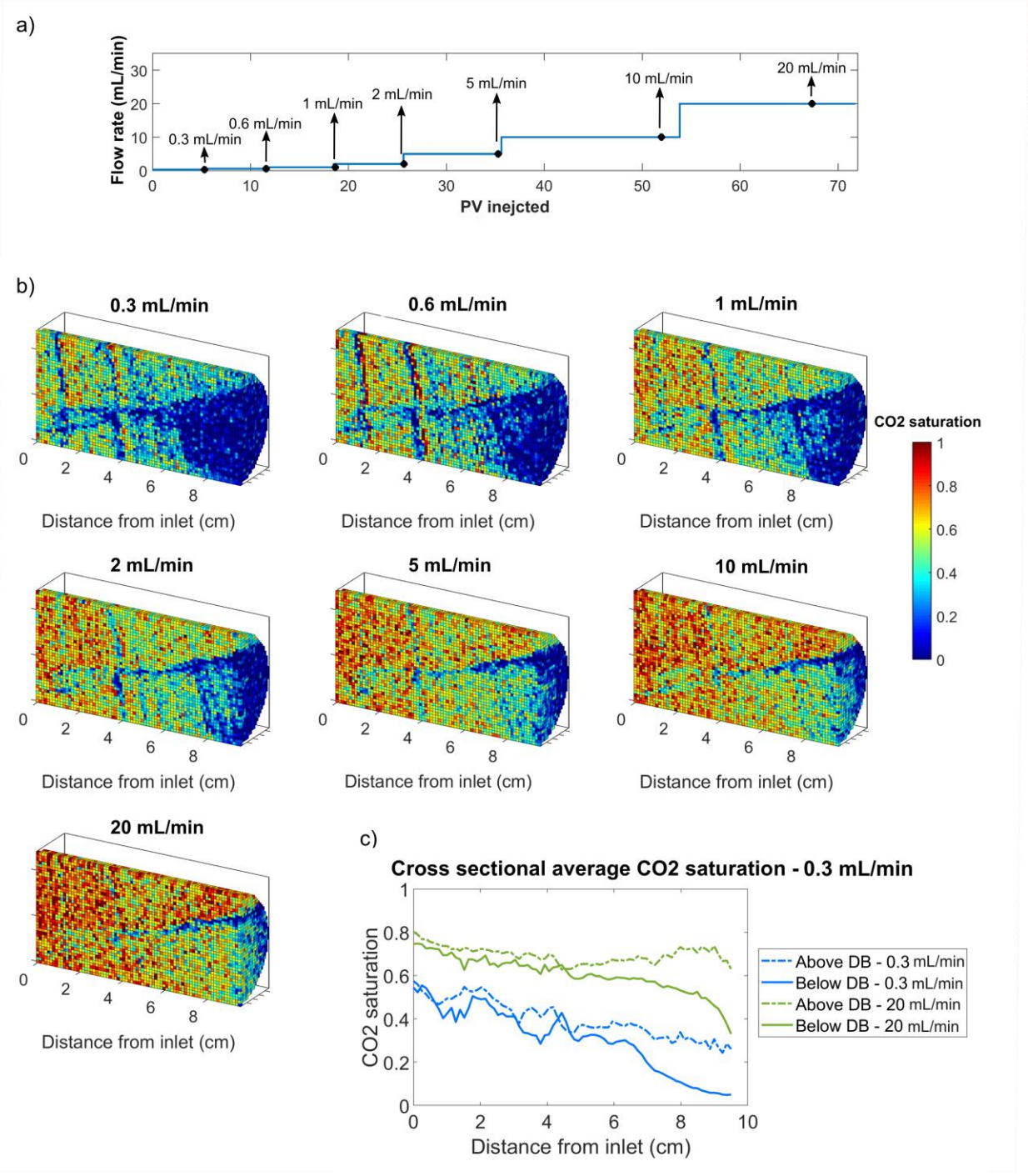

Figure 6. a) Injection strategy for the core flooding drainage experiments. CO_2 was injected in the water saturated sample at progressively higher flow rates of 0.3, 0.6, 1, 2, 5, 10, 20 mL/min. Circle marks corresponds to the scan images taken at steady state conditions for each flow rate. b) CO_2 saturation measured for different flow rates at steady state conditions. Voxel resolution 0.125x0.125x0.125 cm. Grid size is 38x38x76 cells. c) Slice average CO_2 saturation for the compartment below and above the deformation bands (DB) for both flow rates, 0.3 mL/min and 20 mL/min. The difference in saturation between the two compartments is higher towards the

outlet and less pronounced for the highest flow rate. An uncertainty of 0.18 in voxel saturation measurement (σ_S) due to random error of CT number was calculated using methods explained in Pini et al. (2012).

4 Numerical modeling of multiphase flow experiments

Multiphase fluid flow simulations were conducted using the GPRS simulator to fully understand the CO_2 saturation distribution and migration in the presence of deformation bands. The porosity and permeability fields used in the model were those derived in section 3.2 and 3.3. The capillary entry pressure was calculated for each grid block in the model using the Leverett J-function model, which scales the capillary pressure curve derived from the experimental data based on the porosity and permeability distribution (Li, 2011). Water and CO_2 relative permeability curves were calculated using the Brooks-Corey model (Brooks & Corey, 1964). Details of input parameters are included in supporting information (Text S2, Figure S3, S4, S5, Table S2). Given that the bands traverse the full core width, for simplicity, a 2D model was developed (grid size 35X78 cells, pixel resolution 0.125 cm) to model the central rectangular cross-section along the core. The model is initially fully saturated with water prior to injection of CO_2. Boundary conditions (Figure S6 in supporting information) were no flow conditions on the lateral faces, a time-varying CO_2 flow rate, adjusted for cross-sectional area, at the inlet face equal to the experimental flow rate (Figure 6a) and a fixed outlet pressure of 9 MPa.

4.1 Multiphase fluid flow simulation with capillary end effect

In the experimental setup there is a small gap between the core and the outlet cap, which effectively creates a reservoir at the end of the core where the permeability and porosity are very high. This zone creates a capillary pressure discontinuity. A negative gradient of CO_2 saturation (Pini & Benson, 2013) is associated with this "discontinuity of capillarity in the wetting phase" (Huang & Honarpour, 1998), creating a so-called capillary end effect. To simulate this effect, a small reservoir characterized by low capillary entry pressure (0.02 kPa), high porosity (0.7), and high permeability (100000 mD) was placed in the final right-hand column of grid cells at the end of the model.

Simulation results show, for all flow rates, a lower CO_2 saturation in the compartment below the deformation bands than the one above it (Figure 7a). A decreasing CO_2 saturation near the end of the core is also apparent (Figure 7b). As in the experiment, the difference in saturation above and below the bands is higher toward the outlet of the core.

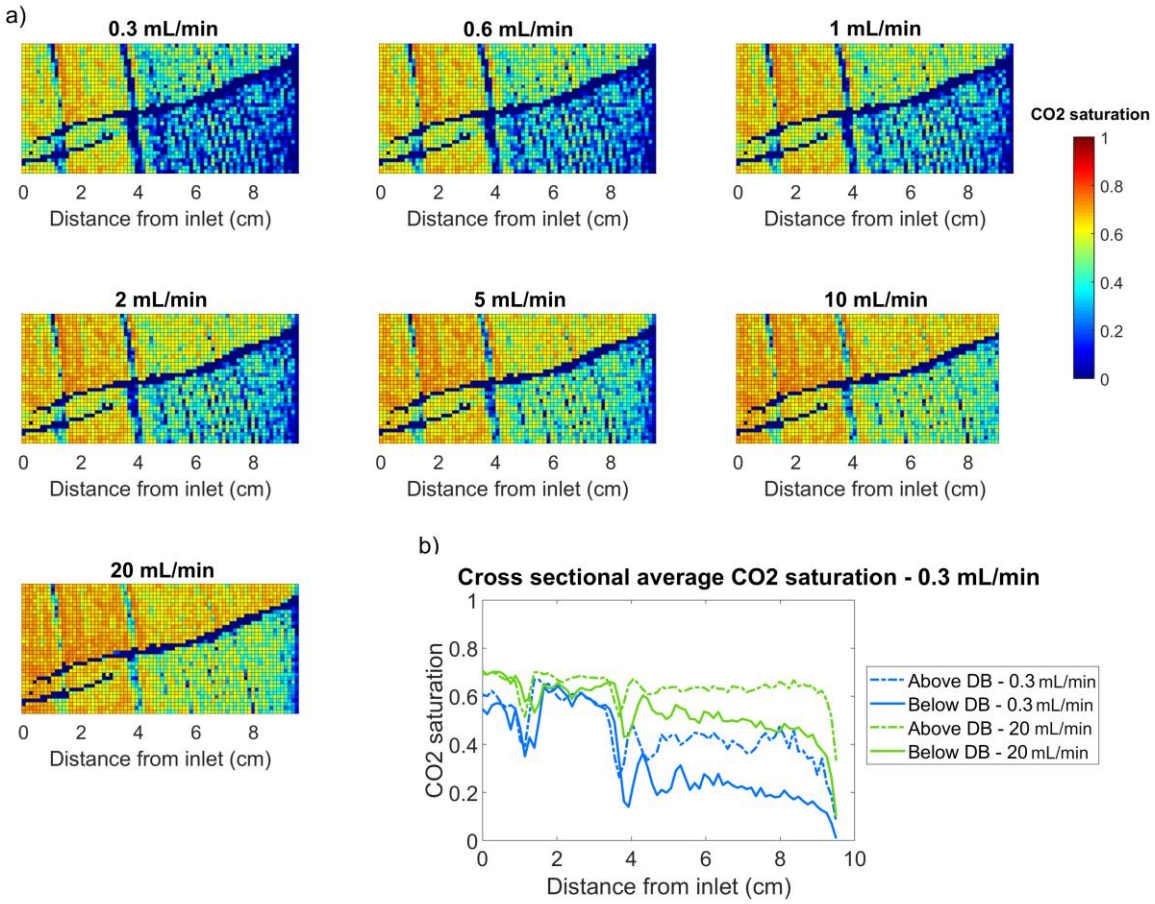

Figure 7. a) Simulation results for the model with small reservoir at the end (capillary end effect). Lower CO_2 saturation is seen in the portion below the deformation bands. b) Comparison between the two compartments at 0.3 mL/min and 20 mL/min. This plot illustrates the negative CO_2 saturation trend due to capillary end effect. For all the flow rates, there is a lower CO_2 saturation in the compartment below the bands compared to above the bands.

The model is able to capture the main characteristics of the experiment, specifically the difference in saturation between the two compartments and the effect of the laminae on CO_2 distribution (Figure 8). At 0.3 mL/min, the model over-predicts the CO_2 saturation towards the outlet (Figure 8 top left). This is likely related to an underestimation in the model of the capillary entry pressure near the outlet. As the viscous pressure drop increases with increasing flow rate, the influence of capillary heterogeneities on fluid saturation distribution decreases. At 2 mL/min (Figure 8 top right) the model agrees with the experimental CO_2 saturation at the outlet of the core, suggesting that the decreasing CO_2 saturation trend in both compartments is strongly influenced by the capillary end effect. At 20 mL/min the model under-predicts the final CO_2 saturation (Figure 8 bottom left). This can be explained by the fact that, during experiments, the capillary end effect has lower extension at high flow rates (Guédon, et al., 2017).

For flow rates higher than 1 ml/min, the simulation results show higher inlet water saturation and therefore lower capillary pressure values as compared to the experimental results (Figure 8 bottom

right). This is probably due to either an overestimation in the model of the capillary entry pressure near the inlet of the core or small errors in the relative permeability used within the model.

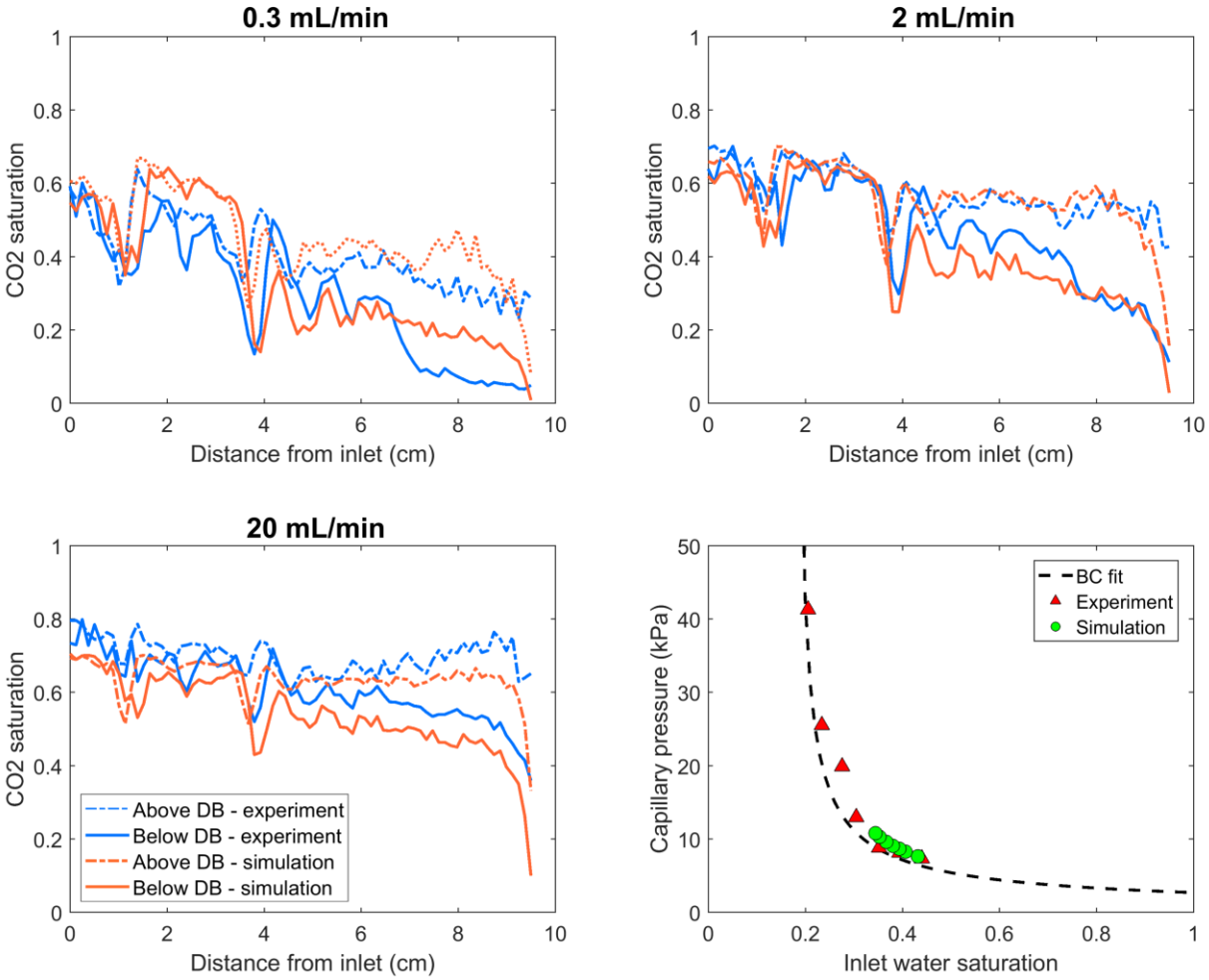

Figure 8. Comparison between experimental (blue) and simulation results (orange) for three different flow rates. The model captures the CO_2 saturation behavior in the experiment at 0.3 mL/min (upper left) and 2 mL/min (upper right). At 0.3 mL/min, the saturation shadow zone seen in the experiment is not replicated in the simulation. At 20 mL/min (lower left) the negative trend shown in the simulation is not representative of the experimental results. (lower right) Inlet capillary pressure values for all flow rates, resulting from experiments and simulations with small reservoir at the end of the core. The capillary pressure in steady state conditions can be assumed to be equal to the differential pressure measured at the inlet slice of the core (Pini, et al., 2012).

4.2 Multiphase fluid flow simulation without the capillary end effect

To exclude the influence of the capillary end effect on the CO_2 saturation distribution, and isolate the impact of the deformation bands, the model was repeated with no small reservoir at the end. Results (Figure 9) show that the deformation bands continue to compartmentalize fluids in the host rock and that the compartment below the bands continues to have a lower saturation than the one above. At 20 mL/min small portions of deformation bands become saturated with CO_2, leading to

cross flow between compartments above and below the bands. As shown in Figures 2, 5 and S5, there is no substantial difference in porosity, absolute permeability or capillary entry pressure between the two compartments. As is the case with single phase flow, the difference in CO_2 saturation can be attributed to the geometry of the two compartments. The compartment above the bands has a smaller cross-sectional area towards the outlet, resulting in a higher fluid velocity and a higher pressure gradient when compared to the compartment below the bands.

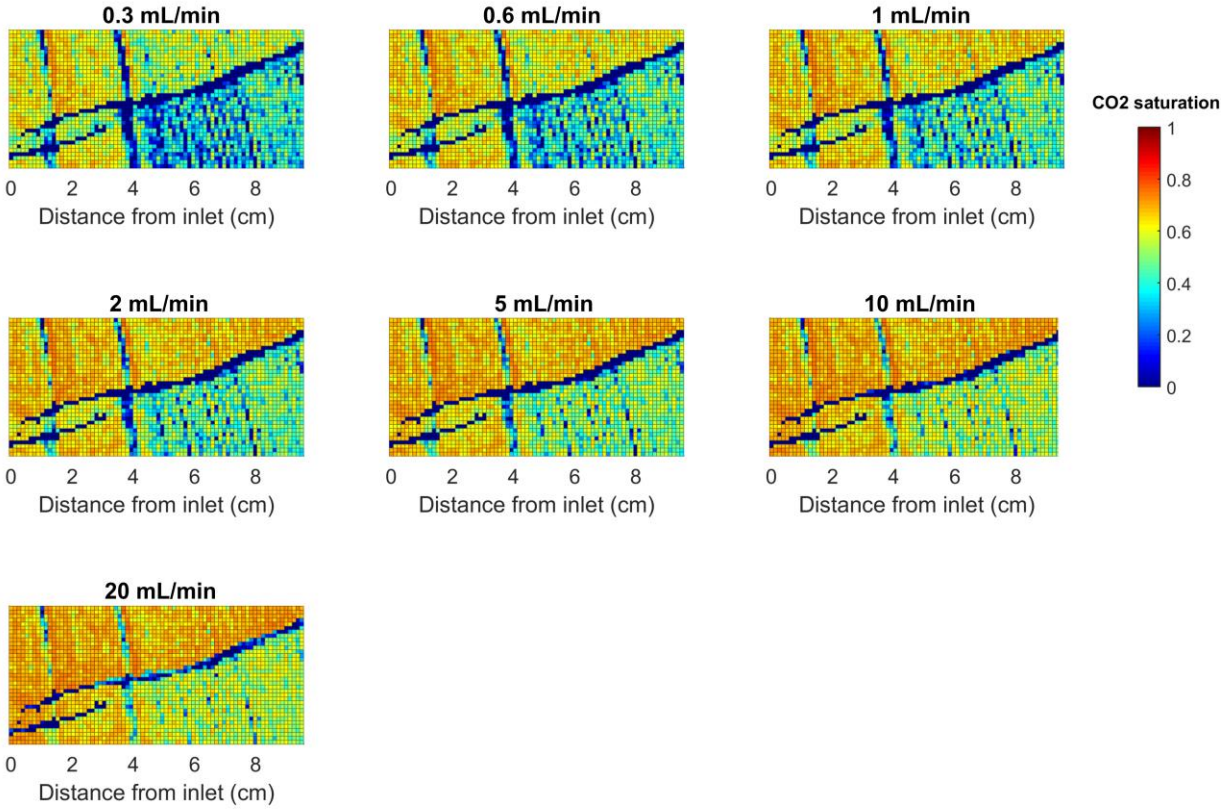

Figure 9. Simulation results for the model without small reservoir at the end (with no capillary end effect). Lower CO_2 saturation is shown in the compartment below the deformation bands. Some portions of the deformation bands are partially saturated with CO_2 at 20 mL/min.

4.3 Multiphase fluid flow simulation without laminae

The experimental observations (Figure 6) show that the laminae have a significant influence on CO_2 migration. To distinguish the relative effects on CO_2 saturation of the deformation bands and the laminae, a simulation was conducted with no end effects and with the laminae removed.

Figure 10 shows CO_2 saturation and capillary pressure distribution with and without the laminae for an injection rate of 0.3 mL/min. This flow rate has been chosen, because the highest influence of laminae on fluid flow has been observed during these drainage flow conditions. With the laminae removed, the difference between the CO_2 saturation above and below the bands is less pronounced; the low saturation levels in the bottom host rock compartment are maintained at the inlet. These results confirm the earlier experimental interpretation that CO_2 saturation increases

upstream of the laminae. This demonstrates that the laminae act as capillary barriers at low flow rates.

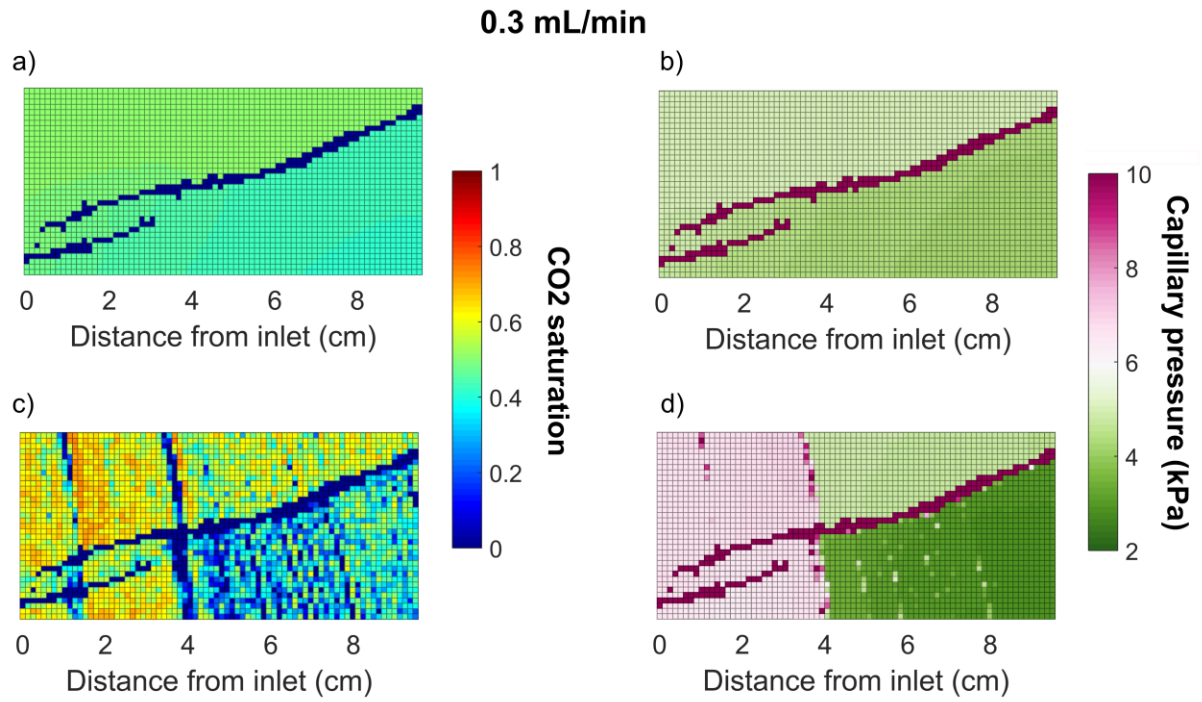

Figure 10. a) CO_2 saturation for the model without end effect and laminae. b) Capillary pressure calculated for the model without end effect and laminae. c) CO_2 saturation for the model of the core without end effect. d) Capillary pressure calculated for the model of the core without end effect. The presence of laminae increases both saturation and capillary pressure for the first 4 cm of the core.

5 Discussion

The effect of cataclastic deformation bands on single and multiphase fluid flow have been investigated *in situ* for the first time. While deformation bands do not entirely surround any individual portion of the host rock in our core sample, we find that they significantly contribute to fluid compartmentalization. Deformation bands subdivide the host rock into two distinct regions, above and below the deformation bands. The compartmentalization results in differing fluid velocity distributions and CO_2 saturation values. The low permeability of the bands, demonstrated by the single phase flow experiments, together with their high capillary entry pressure, significantly inhibit cross-flow of CO_2 between the two compartments.

In our experiments, the deformation bands are sub-parallel to the flow direction and therefore fluid is not forced to travel across them. This results in the deformation bands remaining almost entirely unsaturated with CO_2 and almost no cross-flow occurring. If the deformation bands were oriented perpendicular to the flow, we would expect a different outcome. The grain size distribution within individual laminae is narrow because the Navajo sandstone is aeolian. However, within the deformation bands the particle size distribution is much broader. Figure 11a shows a microscale

image of a deformation band from the Big Hole fault field site. The band is a mixture of larger 'survivor' grains and very fine crushed grain material. This results in almost no residual porosity, since the crushed material entirely fills the gaps between the larger grains (Figure 11b). With deformation bands perpendicular to the flow we would expect an effect similar to that of the finer-grained laminae, but much more pronounced as the entry pressure will be much higher.

To understand the implications of our research for multiphase fluid injection at a commercial scale, it is important to be able to characterize deformation band frequency and orientation within a reservoir. Deformation bands do not generally occur with a unique orientation, or indeed, as single isolated bands; they form conjugate sets (Figure 11c) and are often present in thick anastomosing clusters. This implies a high degree of 3D reservoir anisotropy and the potential for significant CO_2 channeling in lozenge-shaped compartments confined by deformation bands. Lower fluid saturation zones (shadow zones), fluid compartmentalization, injection pressure buildup and preferential channels for fluid migration, are all potential effects of the presence of deformation bands in a sandstone reservoir. Consequently, adequate characterization of petrophysical deformation band properties, through micro-structural analysis or flow experiments, alongside their orientation, thickness, and spatial distribution, through scan-line sampling, well logs and borehole seismic data, are all important factors to consider when estimating the likely storage volume and injection pressure of, for example, a potential CO_2 storage reservoir.

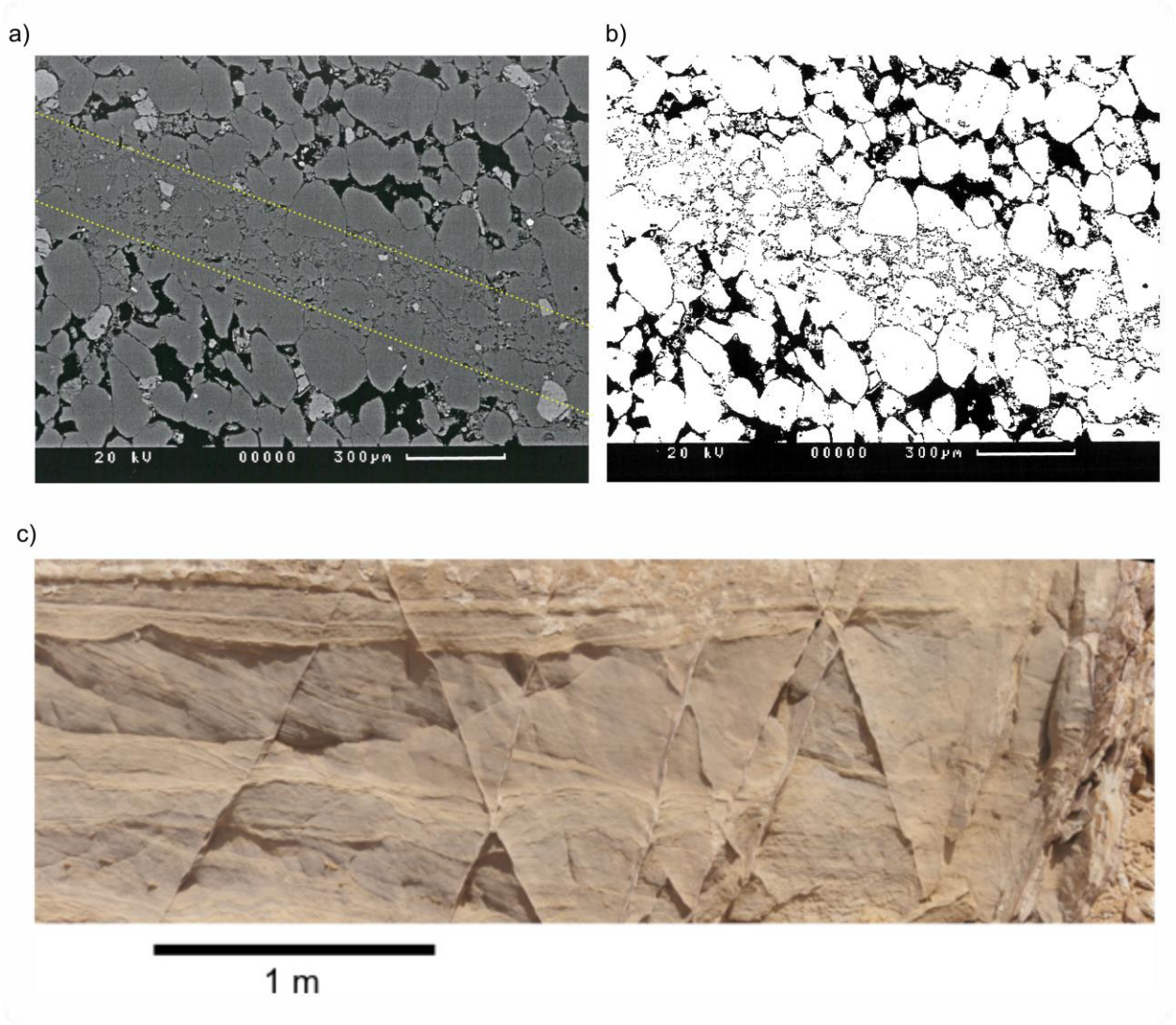

Figure 11. a) BSEM of a deformation band in the Navajo sandstone at the Big Hole Fault. Deformation bands is included in the yellow dashed lines; pores are in black. b) Segmented image of Figure 11a. Smaller grains (white) and pore space (black) along the band. c) Conjugate sets of deformation bands from an outcrop of the Slick Rock Member of Entrada Sandstone in Utah.

6 Conclusions

Single phase and multiphase core flooding experiments were conducted in a sandstone core presenting diagonal cataclastic deformation bands and two lower-porosity laminae. In the single phase experiment, PET imaging revealed that the presence of the diagonal deformation bands created a strong difference in the velocity distributions between compartments of the host rock above and below the deformation bands. This difference was not caused by any difference in porosity and permeability between the two compartments, but instead was attributed to the geometry of the band. No effect of the laminae on single phase flow transport was apparent.

High-pressure CO_2 injection drainage experiments were conducted in the same core and imaged with a medical X-ray CT scanner, allowing progressive imaging of CO_2 saturation at different flow

rate conditions. Results show that both the finer-grained laminae and the deformation bands acted as capillary barriers. The laminae form weaker capillary barriers than the deformation bands, with the compartment below the bands presenting lower CO_2 saturation for all flow rates, particularly toward the outlet. Numerical simulations of the experiments at low flow rates revealed that while some of the low saturation at the outlet was due to the experimental capillary end effect simulations without the end effect also predicted significant differences in CO_2 saturation due to the presence of the bands. Deformation bands have extremely low permeability and porosity, and a very high capillary entry pressure that inhibits CO_2 migration across the bands. The bands remained saturated with water during the experiments, contributing to the isolation of the two host rock compartments.

At the reservoir scale, deformation bands form conjugate sets and are often present in thick anastomosing clusters. Thus, deformation bands have the potential to channel and compartmentalize both single and multiphase fluid flow. These findings have important consequences for predicting multiphase flow in sandstone reservoirs and specific implications for storage capacity and injectivity of carbon and storage in geological formation.

Acknowledgments

The authors would like to thank Prof. James P. Evans for providing us the core sample, Dr Maartje Boon for her assistance using the GPRS simulator and Dr Yannick Kremer for the Figure 11c. All data underpinning this publication are openly available from the University of Strathclyde KnowledgeBase at https://doi.org/10.15129/a0f905b5-1e5b-4d7a-ab45-880b3c3f55c3. The experimental work was funded in part by the Global Climate Energy Project. The Inveon DPET (preclinical PET) scanner was funded by NIH grant number 1S10OD018130-01.

References

Akbarabadi, M. & Piri, M., 2013. Relative permeability hysteresis and capillary trapping characteristics of supercritical CO2/brine systems: An experimental study at reservoir conditions. *Advances in Water Resources,* Volume 52, pp. 190-206.

Akin, S. & Kovscek, A. R., 2003. Computed tomography in petroleum engineering research. *Geological Society, London, Special Publications,* Volume 215(1), pp. 23-38.

Antonellini, M. & Aydin, A., 1994. Effect of faulting on fluid flow in porous sandstones: petrophysical properties. *AAPG bulletin,* Volume 78(3), pp. 355-377.

Aydin, A., 1978. Small faults formed as deformation bands in sandstone. *Rock Friction and Earthquake Prediction,* pp. 913-930.

Aydin, A., Borja, R. I. & Eichhubl, P., 2006. Geological and mathematical framework for failure modes in granular rock. *Journal of Structural Geology,* Volume 28(1), pp. 83-98.

Aydin, A. & Johnson , A. M., 1978. Development of faults as zones of deformation bands and as slip surfaces in sandstone. *Pure and applied Geophysics,* Volume 116(4-5), pp. 931-942.

559 Ballas, G., Fossen, H. & Soliva, R., 2015. Factors controlling permeability of cataclastic
560 deformation bands and faults in porous sandstone reservoirs. *Journal of Structural Geology*,
561 Volume 76, pp. 1-21.

562 Benson, S. & Cook, P., 2005. *Chapter 5: Underground geological storage,* Interlachen,
563 Switzerland: IPCC Special Report on Carbon Dioxide Capture and Storage, Intergovernmental
564 Panel on Climate Change.

565 Bjørlykke, K. & Jahren, J., 2010. Sandstones and sandstone reservoirs. *Petroleum Geoscience*,
566 Issue Springer, Berlin, Heidelberg, pp. 113-140.

567 Bloomfield, J., Gooddy, D., Bright, M. & Williams, P., 2001. Pore-throat size distributions in
568 Permo-Triassic sandstones from the United Kingdom and some implications for contaminant
569 hydrogeology. *Hydrogeology Journal,* Volume 9(3), pp. 219-230.

570 Boon, M., Ni, H., Garing, C. & Benson, S. M., 2018. *Effect of Capillary Induced Flow on Co2*
571 *Residual Trapping.* Melbourne, 14th Greenhouse Gas Control Technologies Conference, pp. 21-
572 26.

573 Brooks, R. H. & Corey, A. T., 1964. Hydraulic properties of porous media. *Hydrology*
574 *Papers,Colorado State University,* Volume 24, p. 37.

575 Cao, H., 2002. *Development of techniques for general purpose simulators*. Doctoral dissertation,
576 Stanford University.

577 Cao, H. & Aziz, K., 2002. *Performance of IMPSAT and IMPSAT-AIM models in compositional*
578 *simulation.* In SPE Annual Technical conference and Exhibition, Society of Petroleum Engineers.

579 Cashman, S. & Cashman, K., 2000. Cataclasis and deformation-band formation in unconsolidated
580 marine terrace sand, Humboldt County, California. *Geology,* Volume 8(2), pp. 111-114.

581 Corey, A. T. & Rathjens, C. H., 1956. Effect of stratification on relative permeability. *Journal of*
582 *Petroleum Technology,* Volume 8(12), pp. 69-71.

583 Fossen, H., Schultz, R., Shipton, Z. K. & Mair, K., 2007. Deformation bands in sandstone: a
584 review. *Journal of the Geological Society,* Volume 164(4), pp. 755-769.

585 Garing, C. & Benson, S. M., 2019. CO2 Wettability of Sandstones: Addressing Conflicting
586 Capillary Behaviors. *Geophysical Research Letters,* Volume 46(2), pp. 776-782.

587 Grathwohl, P. & Kleineidam, S., 1995. Impact of heterogeneous aquifer materials on sorption
588 capacities and sorption dynamics of organic contaminants. *AHS Publications-Series of*
589 *Proceedings and Reports-Intern Assoc Hydrological Sciences,* Volume 79-86, p. 225.

590 Guédon, G. R. et al., 2017. Influence of capillary end effects on steady-state relative permeability
591 estimates from direct pore-scale simulations. *Physics of Fluids,* Volume 29(12), p. 123104.

592 Hingerl, F. F. et al., 2016. Characterization of heterogeneity in the Heletz sandstone from core to
593 pore scale and quantification of its impact on multi-phase flow. *International Journal of*
594 *greenhouse gas control,* Volume 48, pp. 69-83.

595 Huang, D. D. & Honarpour, M. M., 1998. Capillary end effects in coreflood calculations. *Journal*
596 *of Petroleum Science and Engineering,* Volume 19(1-2), pp. 103-117.

597 Jiang, Y., 2008. *Techniques for modeling complex reservoirs and advanced wells.* Doctoral
598 dissertation, Stanford University.

599 Kim, K. Y. et al., 2018. Two-phase flow visualization under reservoir conditions for highly
600 heterogeneous conglomerate rock: A core-scale study for geologic carbon storage. *Scientific*
601 *reports,* Volume 8(1), p. 4869.

602 Krause, M. H., 2012. *Modeling and investigation of the influence of capillary heterogeneity on*
603 *relative permeability.* In SPE Annual Technical Conference and Exhibition, Society of Petroleum
604 Engineers.

605 Krause, M., Krevor, S. & Benson, S. M., 2013. A procedure for the accurate determination of sub-
606 core scale permeability distributions with error quantification. *Transport in porous media,* Volume
607 98(3), pp. 565-588.

608 Krevor, S. et al., 2015. Capillary trapping for geologic carbon dioxide storage–From pore scale
609 physics to field scale implications. *International Journal of Greenhouse Gas Control,* Volume 40,
610 pp. 221-237.

611 Krevor, S. C., Pini, R., Li, B. & Benson, S. M., 2011. Capillary heterogeneity trapping of CO2 in
612 a sandstone rock at reservoir conditions. *Geophysical Research Letters,* Volume 38(15).

613 Krevor, S. C., Pini, R., Zuo, L. & Benson, S. M., 2012. Relative permeability and trapping of CO2
614 and water in sandstone rocks at reservoir conditions. *Water Resources Research,* Volume 48(2).

615 Kruth, J. P. et al., 2011. Computed tomography for dimensional metrology. *CIRP Annals-*
616 *Manufacturing Technology,* 60(2), pp. 821-842.

617 Li, B., 2011. *Including fine-scale capillary heterogeneity in modeling the flow of CO2 and brine*
618 *in reservoir cores.* Doctoral dissertation, Stanford University.

619 Li, B. & Benson, S. M., 2015. Influence of small-scale heterogeneity on upward CO2 plume
620 migration in storage aquifers. *Advances in Water Resources,* Volume 83, pp. 389-404.

621 Li, B., Benson, S. M. & Tchelepi, H. A., 2012. *Modeling fine-scale capillary heterogeneity in*
622 *multiphase flow of CO2 and brine in sedimentary rocks.* University of Illinois at Urbana-
623 Champaign, IL, USA, Proceedings of the XIX International Conference on Water Resources.

624 Li, Y. et al., 2019. Investigation of the Dynamic Capillary Pressure during Displacement Process
625 in Fractured Tight Rocks. *AIChE Journal.*

626 Manzocchi, T., Heath, A. E., Walsh, J. J. & Childs, C., 2002. The representation of two phase
627 fault-rock properties in flow simulation models. *Petroleum Geoscience,* Volume 8(2), pp. 119-
628 132.

629 McGrath, A. G. & Davison, I., 1995. Damage zone geometry around fault tips. *Journal of*
630 *Structural Geology,* Volume 17(7), pp. 1011-1024.

631 Medina, C. R., Rupp, J. A. & Barnes, D. A., 2011. Effects of reduction in porosity and permeability
632 with depth on storage capacity and injectivity in deep saline aquifers: A case study from the Mount
633 Simon Sandstone aquifer. *International journal of greenhouse gas control,* Volume 5(1), pp. 146-
634 156.

635 Naff, R. L., 1990. Arrival times and temporal moments of breakthrough curves for an imperfectly
636 stratified aquifer. *Water Resources Research,* Volume 28(1), pp. 53-68.

637 Ni, H., Boon, M., Garing, C. & Benson, S. M., 2019. Predicting CO2 residual trapping ability
638 based on experimental petrophysical properties for different sandstone types. *International*
639 *Journal of Greenhouse Gas Control,* Volume 86, pp. 158-176.

640 Ochi, J. & Vernoux, J. F., 1998. Permeability decrease in sandstone reservoirs by fluid injection:
641 hydrodynamic and chemical effects. *Journal of hydrology,* Volume 208(3-4), pp. 237-248.

642 Ogilvie, S. R., Orribo, J. M. & Glover , P. W. J., 2001. The influence of deformation bands upon
643 fluid flow using profile permeametry and positron emission tomography. *Geophysical Research*
644 *Letters,* Volume 28(1), pp. 61-64.

645 Pasala, S. M., Forster, C. B., Deo, M. & Evans, J. P., 2013. Simulation of the impact of faults on
646 CO 2 injection into sandstone reservoirs. *Geofluids,* Volume 13(3), pp. 344-358.

647 Perrin, J. C. & Benson, S., 2010. An experimental study on the influence of sub-core scale
648 heterogeneities on CO2 distribution in reservoir rocks. *Transport in porous media,* Volume 82(1),
649 pp. 93-109.

650 Perrin, J. C. et al., 2009. Core-scale experimental study of relative permeability properties of CO2
651 and brine in reservoir rocks. *Energy Procedia,* Volume 1(1), pp. 3515-3522.

652 Pini, R. & Benson, S. M., 2013. Simultaneous determination of capillary pressure and relative
653 permeability curves from core-flooding experiments with various fluid pairs. *Water Resources*
654 *Research,* Volume 49(6), pp. 3516-3530.

655 Pini, R. & Benson, S. M., 2017. Capillary pressure heterogeneity and hysteresis for the
656 supercritical CO2/water system in a sandstone. *Advances in Water Resources,* Volume 108, pp.
657 277-292.

658 Pini, R., Krevor, S. C. & Benson, S. M., 2012. Capillary pressure and heterogeneity for the
659 CO2/water system in sandstone rocks at reservoir conditions. *Advances in Water Resources,*
660 Volume 38, pp. 48-59.

661 Qu, D. & Tveranger, J., 2016. Incorporation of deformation band fault damage zones in reservoir
662 models. *AAPG Bulletin,* Volume 100(3), pp. 423-443.

663 Rawling, G. C. & Goodwin, L. B., 2003. Cataclasis and particulate flow in faulted, poorly lithified
664 sediments. *Journal of Structural Geology,* Volume 25(3), pp. 317-331.

665 Rotevatn, A. & Fossen, H., 2011. Simulating the effect of subseismic fault tails and process zones
666 in a siliciclastic reservoir analogue: Implications for aquifer support and trap definition. *Marine*
667 *and Petroleum Geology,* Volume 28(9), pp. 1648-1662.

668 Rotevatn, A. et al., 2017. Do deformation bands matter for flow? Insights from permeability
669 measurements and flow simulations in porous carbonate rocks. *Petroleum Geoscience,* Volume
670 23(1), pp. 104-119.

671 Ruprecht, C. et al., 2014. Hysteretic trapping and relative permeability of CO2 in sandstone at
672 reservoir conditions. *International Journal of Greenhouse Gas Control,* Volume 27, pp. 15-27.

673 Saadatpoor, E., Bryant, S. L. & Sepehrnoori, K., 2010. New trapping mechanism in carbon
674 sequestration. *Transport in porous media,* Volume 82(1), pp. 3-17.

675 Schueller, S., Braathen, A., Fossen, H. & Tverang, J., 2013. Spatial distribution of deformation
676 bands in damage zones of extensional faults in porous sandstones: Statistical analysis of field data.
677 *Journal of Structural Geology,* Volume 52, pp. 148-162.

678 Schultz, R. A. & Siddharthan, R., 2005. A general framework for the occurrence and faulting of
679 deformation bands in porous granular rocks. *Tectonophysics,* Volume 411(1-4), pp. 1-18.

680 Shipton, Z. K. & Cowie, P. A., 2001. Damage zone and slip-surface evolution over μm to km
681 scales in high-porosity Navajo sandstone, Utah. *Journal of Structural Geology,* Volume 23(12),
682 pp. 1825-1844.

683 Shipton, Z. K. & Cowie, P. A., 2003. A conceptual model for the origin of fault damage zone
684 structures in high-porosity sandstone. *Journal of Structural Geology,* Volume 25, p. 333–345.

685 Shipton, Z. K., Evans, J. B. & Thompson, L. B., 2005. The geometry and thickness of deformation
686 band fault core, and its influence on sealing characteristics of deformation band fault zones.
687 *American Association of Petroleum Geologists Memoir,* Volume 85, pp. 181-195.

688 Shipton, Z. K. et al., 2002. Structural heterogeneity and permeability in faulted eolian sandstone:
689 Implications for subsurface modeling of faults. *AAPG bulletin,* Volume 86(5), pp. 863-883.

690 Taylor, W. L. & Polland, D. D., 2000. Estimation of in situ permeability of deformation bands in
691 porous sandstone, Valley of Fire, Nevada. *Water Resources Research,* Volume 36(9), pp. 2595-
692 2606.

693 Torabi, A., Fossen, H. & Braathen, A., 2013. Insight into petrophysical properties of deformed
694 sandstone reservoirs. *Aapg Bulletin, 9,* Volume 97(4), pp. 619-637.

Tueckmantel, C. et al., 2012. Two-phase fluid flow properties of cataclastic fault rocks: Implications for CO2 storage in saline aquifers. *Geology,* Volume 40(1), pp. 39-42.

Vasco, D. W., Pride, S. R., Zahasky, C. & Benson, S. M., 2018. Calculating trajectories associated with solute transport in a heterogeneous medium. *Water Resources Research,* Volume 54(9), pp. 6890-6908.

Vinegar, J. H. & Wellington, S. L., 1987. Tomographic imaging of three-phase flow experiments. *Review of Scientific Instruments,* Volume 58(1), pp. 96-107.

Wellington, S. L. & Vinegar, H. J., 1987. X-ray computerized tomography. *Journal of Petroleum Technology,* Volume 39(08), pp. 885-898.

Wilkins, S. J., Davies , R. K. & Naruk, S. J., 2019. Subsurface Observations of Deformation Bands and Their Impact on Hydrocarbon Production within the Holstein Field, Gulf of Mexico, USA. *Geological Society, London,* Volume Special Publications, 496, pp. SP496-2018.

Withjack, E. M., 1988. Computed tomography for rock-property determination and fluid-flow visualization. *SPE formation evaluation,* Volume 3(04), pp. 696-704.

Zahasky, C. & Benson, S. M., 2018. Micro-positron emission tomography for measuring sub-core scale single and multiphase transport parameters in porous media. *Advances in Water Resources,* Volume 115, pp. 1-16.

Zahasky, C., Kurotori, T., Pini, R. & Benson, S. M., 2019. Positron emission tomography in water resources and subsurface energy resources engineering research. *Advances in Water Resources,* Volume 127, pp. 39-52.